ELSEVIER

International Journal of Heat and Fluid Flow 19 (1998) 533–540

International Journal of HEAT AND FLUID FLOW

Compression of a turbulent vortex flow

O.Le Roy, L.Le Penven *

Laboratoire de Mécanique des Fluides et d'Acoustique, UMR 5509, ECL-UCB-CNRS, Ecole Centrale de Lyon, 36, avenue Guy de Collongue, BP 163-69131 Ecully Cedex, France

Abstract

Reynolds-averaged Navier–Stokes equations are used in conjunction with different turbulence models to simulate the evolution of a turbulent vortex flow submitted to a compression in a direction normal to its axis. A simplified configuration is considered idealizing important flow features observed in Internal Combustion engines (tumbling flows). Strong differences are observed between predictions of k–ε and Reynolds stress models. Comparison to the experimental data obtained recently by Marc et al. (Marc, D., Borée, J., Bazile, R., Charnay, G., 1997. In: 11th Symposium on Turbulent Shear Flows. Grenoble, France; SAE paper 972834), indicates a better agreement for the latter. The possible existence of precession motion of the vortex core and a three-dimensional evolution for the mean flow are also discussed using direct numerical simulations of a simplified vortex (Taylor vortex).

1. Introduction

In recent years, much effort has been devoted by car manufacturers to control the turbulent flow in internal engines in order to improve mixing and combustion. One promising way is to generate during the intake process a large-scale vortical motion whose axis is perpendicular to piston velocity (tumbling flow). In this case, it is observed that the mean vortex breaks up at some stage of the compression and produces a high level of turbulence. This phenomenon improves the mixing and the burning rate significantly. There is not yet a clear explanation for the vortex breakdown. Moreover, we do not know much about the ability of standard turbulence models to predict the observed evolution.

The purpose of this paper is

- to present numerical simulations of a turbulent tumbling flow using the Reynolds-averaged flow equations and different classes of turbulence models (k–ε models, $\overline{u_i u_j}$–ε models).
- to interpret the evolution of the mean flow during compression by comparison to laminar computations of a simplified vortex (Taylor–Green vortex) with different boundary conditions (no-slip, no shear).

Despite the long history of Reynolds stress modelling, it must be noted that applications to internal engine flows are relatively recent (Watkins et al., 1991; Watkins and Bo, 1996; Lea and Watkins, 1997; Lebrère et al., 1996). This class of flows displays a rather specific combination of typical features: unsteadiness, high confinement, rotation and compression effects so that comparison to new experimental data still remains instructive. The present work is a contribution to this effort.

2. Test flow configuration

The geometry considered for numerical simulations corresponds to the experiment of Marc et al. (1997a) (hereafter: IMFT experiment) (Fig. 1). The flow develops in a chamber equipped with a square piston moving alternatively with the velocity

$$Vp = Vp_{\max} \sin(\omega t), \quad Vp_{\max} = 0.9 \text{ m s}^{-1}, \tag{1}$$

$$\omega = 220 \text{ rev/min}. \tag{2}$$

At top dead center ($\omega t = 0°$), the intake canal flow is accelerated by the piston motion and creates a tumbling flow in the chamber. At bottom dead center ($\omega t = 180°$) the chamber is a cube of edge $b = 10$ cm, the intake canal is closed and the compression starts. The compression ratio is $b/a = 5$.

3. Numerical simulations with turbulence models

3.1. Numerics

The Reynolds-averaged equations have been solved numerically assuming that the flow be two-dimensional in the plane x, y. We have used an elliptic solver of the Navier–Stokes equations employing a finite element discretisation on a moving grid, a semi-implicit time-stepping ensuring linearisation of the differential operators and a convection scheme based on the streamline upwind finite element technique (Mao et al., 1994). Walls are assumed athermal, and temperature and density uniform throughout the flow. Typically, the mesh has 25 000 nodes. Turbulence models are standard ones: k–ε model and $\overline{u_i u_j}$–ε model (RSM). For near wall layers, these models are used in conjunction with wall functions and an algebraic model to evaluate the components of the Reynolds tensor (Debaty, 1994).

* Corresponding author. E-mail: lepenven@mecaflu.ec-lyon.fr.

0142-727X/98/$ – see front matter
PII: S0142-727X(98)10028-0

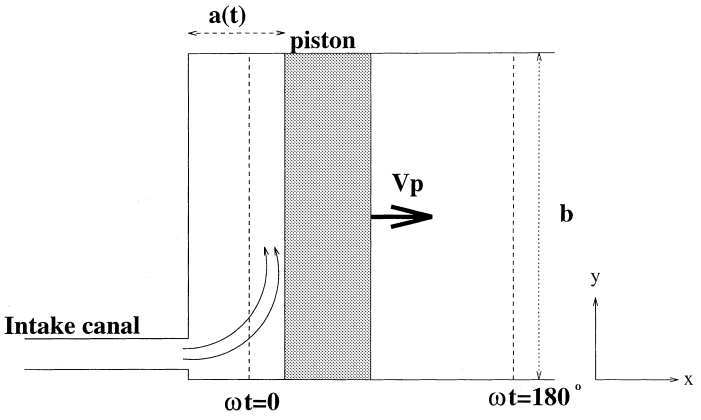

Fig. 1. Geometry of the IMFT experiment.

3.2. Turbulence modelling

The equations for the k–ε model read

$$\frac{Dk}{Dt} = \frac{\partial}{\partial x_j}\left[\left(\nu + \frac{\nu_t}{\sigma_k}\right)\frac{\partial k}{\partial x_j}\right] - \overline{u_i u_j}\frac{\partial U_i}{\partial x_j} - \varepsilon, \tag{3}$$

$$\frac{D\varepsilon}{Dt} = \frac{\partial}{\partial x_j}\left[\left(\nu + \frac{\nu_t}{\sigma_\varepsilon}\right)\frac{\partial \varepsilon}{\partial x_j}\right] - c_{\varepsilon 1}\frac{\varepsilon}{k}\overline{u_i u_j}\frac{\partial U_i}{\partial x_j} - c_{\varepsilon 2}\frac{\varepsilon^2}{k} + c_{\varepsilon 3}S_{ll}\varepsilon, \tag{4}$$

where D/Dt stands for the material derivative following the mean velocity field. The Reynolds tensor is related to the mean strain S_{ij} by the means of an eddy viscosity coefficient $\nu_t = c_\mu k^2/\varepsilon$

$$-\overline{u_i u_j} + \frac{2}{3}k\delta_{ij} = \nu_t\left(S_{ij} - \frac{1}{3}S_{ll}\delta_{ij}\right). \tag{5}$$

We used standard values for the constants: $c_\mu = 0.09$, $c_{\varepsilon 1} = 1.44$, $c_{\varepsilon 2} = 1.92$, $\sigma_k = 1.0$, $\sigma_\varepsilon = 1.3$, $c_{\varepsilon 3} = -\frac{4}{3} + \frac{2}{3}c_{\varepsilon 1}$.

In $\overline{u_i u_j}$–ε model, the Reynolds tensor equation is written as

$$\frac{D\overline{u_i u_j}}{Dt} = P_{ij} + \Phi_{ij} + d_{ij} - \frac{2}{3}\varepsilon\delta_{ij}. \tag{6}$$

The production term P_{ij} is treated exactly

$$P_{ij} = -\overline{u_i u_k}\frac{\partial U_j}{\partial x_k} - \overline{u_j u_k}\frac{\partial U_i}{\partial x_k}. \tag{7}$$

The turbulent transport d_{ij} is modelled using a turbulent diffusion hypothesis

$$d_{ij} = \frac{\partial}{\partial x_k}\left(\frac{\nu t}{\sigma_k}\frac{\partial \overline{u_i u_j}}{\partial x_k}\right). \tag{8}$$

The pressure–strain correlation is split into three contributions

$$\Phi_{ij} = \Phi^1_{ij} + \Phi^2_{ij} + \Phi^w_{ij}. \tag{9}$$

The so-called slow and rapid parts Φ^1_{ij} and Φ^2_{ij} are modelled following Launder et al. (1975). Φ^w_{ij} is a correction depending on the distance to the solid boundaries ("wall echo" term). The main effect of this term is to transfer some part of the normal fluctuation to the direction parallel to the wall. For the present purpose, this term is expected to be of some importance especially at top dead center. We use for Φ^w_{ij} the proposal of Craft and Launder (1991) instead of the more popular Gibson–Launder model (Gibson and Launder, 1978), since it has been proved to give the correct sign of transfer in the case of mean strain normal to the wall (wall impinging jets, piston-induced compression). Finally, it must be noted that the expressions for k–ε model and RSM are modified to account for effects of a mean compression (Serre, 1994; Le Penven and Serre, 1996). A first correction is made on the dissipation equation in which we include the term $c_{\varepsilon 3}S_{ll}\varepsilon$ representative of the increase of mean square vorticity ε/ν due to the volume reduction (Reynolds, 1980). In addition, the mean gradient $U_{i,j}$ is replaced by its non-isotropic (and incompressible) part: $U_{i,j} - U_{k,k}\delta_{ij}/3$ in the expression for the linear part of pressure–strain correlations.

3.3. Results

3.3.1. Intake flow

At the end of the intake, both models predict a well-defined vortex dominating the entire flow field (see the velocity field in Fig. 2). A slight difference is observed on the mean angular momentum which is 30% higher for the k–ε model. As shown in Fig. 3(a) and (b) the mean vorticity distribution predicted by the $\overline{u_i u_j}$–ε model results from the roll-up of the mixing layer produced in the upper edge of the intake jet. The spiral shape is not discernible in the k–ε model predictions and the vortex core motion looks like a solid body rotation.

Fig. 4(a) shows the evolutions of the averaged value of k calculated over the entire chamber. During the first half of the intake, both models predict an increase in k caused by the acceleration of the piston, afterwards k decreases. A striking feature is that kinetic energy is significantly higher in the case of k–ε model. The most important difference is observed at the end of intake. At this time, the ratio of the two predicted levels is about 4. Kinetic energy levels at the end of the intake are shown in Fig. 3(c) and (d). Both models behave similarly. The maxima of k are associated to an increase in the fluctuation normal to the wall in the jet impact zones. A minimum is observed in the vortex core. This minimum is more pronounced in the case of RSM model.

The differences observed in the middle of the chamber can be explained in part by the effects of the mean rotation. To a large extent, the kinetic energy in the core of the vortex results from production effect by the mean shear in the upper edge of the intake jet. In this mixing layer, the streamlines curvature has a stabilizing effect on turbulence and leads to a decrease in turbulent production. Indeed, these effects appear in the Reynolds stress equation through the production term and the pressure–strain correlations. In contrast, because of the use of eddy viscosity hypothesis, the k–ε model gives a production term insensitive to the mean rotation (for example: Speziale et al., 1990).

3.3.2. Compression

At the beginning of compression, both models predict an acceleration of the vortex due to the reduction of the chamber

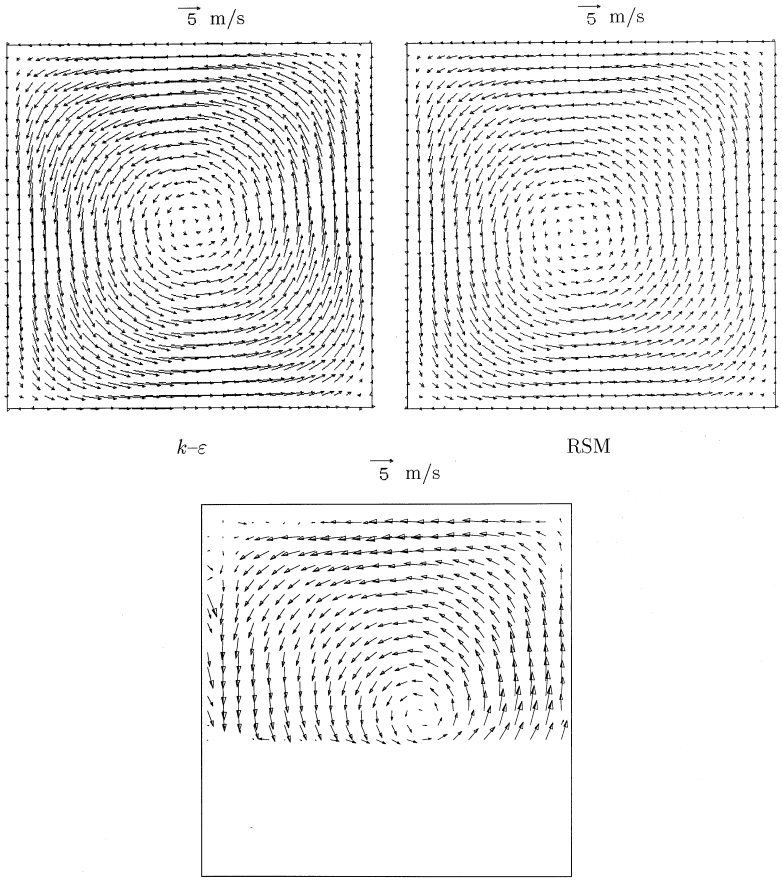

Fig. 2. Comparison models/experiment for velocity fields at $\omega t = 180°$.

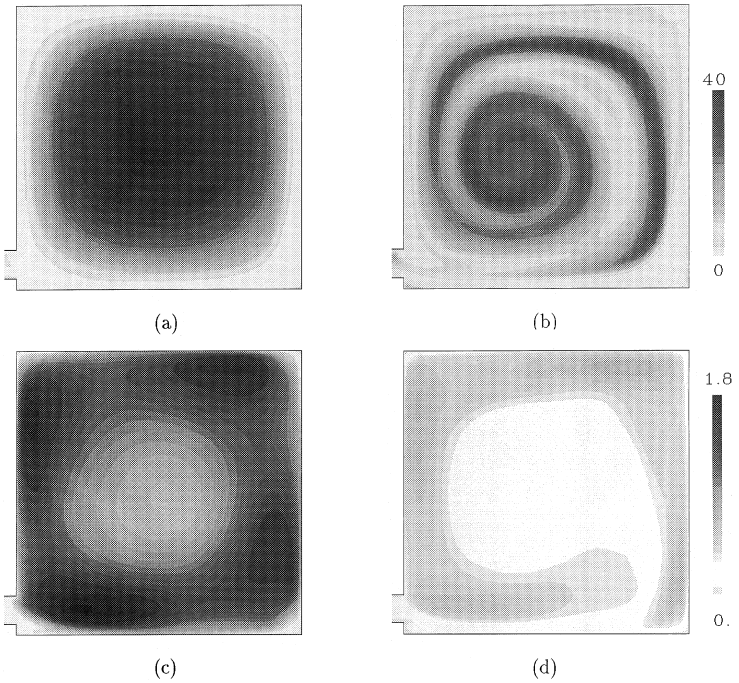

Fig. 3. 180°. (a) Normalized vorticity $\Omega a/Vp_{max}$: k–ε. (b) RSM. (c) Normalized kinetic energy k/Vp^2_{max}: k–ε. (d) RSM.

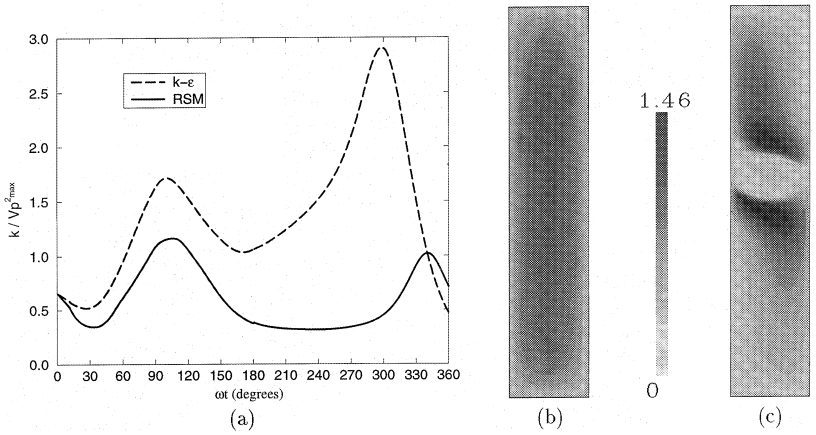

Fig. 4. Evolution of the averaged value of kinetic energy. (a) Normalized kinetic energy k/Vp^2_{max} at $\omega t = 360°$. (b) k–ε. (c) RSM.

volume associated to an increase of kinetic energy. Between 300° and 330°, the $\overline{u_iu_j}$–ε model predicts a separation of the wall layers in the upper right corner and in the lower left corner which are adverse pressure gradient regions then the generation of two vortical structures above and below the initial vortex. These vortices are very intense and have an opposite rotation sign relative to the original vortex (Fig. 5). They spread in the chamber until the end of compression and simultaneously the initial vortex becomes smaller and is confined in the middle of the chamber with a quasi circular shape (Fig. 5). The generation of the two intense vortices involved important velocity gradients and leads to an increase of k level (Fig. 4(c)).

With the k–ε model no separation occurs. We obtain at the same time a strong decrease in the tumble intensity involving the dissociation of the initial vortex in a pair of slow eddies with the same rotation sign (Fig. 5) at the edges of the chamber. This collapse is associated to a strong decrease in the kinetic energy.

3.3.3. Comparison with the IMFT experiment

The experimental data obtained by Marc et al. (1997b) are now compared to the models predictions. As shown in Fig. 2, the experimental mean velocity field obtained from PIV measurements is very similar to the models predictions at the end of intake. The absence of appreciable mean velocity (Marc et al., 1997a) in the spanwise direction at this time gives support to the two-dimensional flow assumption used for the computations. The profiles of U, V, $\overline{u^2}$ and $\overline{v^2}$ are taken along the median axes at the end of intake (Fig. 6). Concerning the mean velocity (Fig. 6(a)), the nearly linear profiles predicted by the k–ε model overestimate the data especially near the walls and a better agreement is obtained from the RSM model. Clearly both models fail to predict the maximum of $\overline{u^2}$ measured in the center of the chamber (Fig. 6(b)). Similar peaks have been detected in the IMFT experiment on x profiles (not shown here). Discarding this local anomaly that will be discussed at the end of the paper, the overall tendency is that the k–ε model overestimates the turbulence levels especially near the walls and that the RSM predictions are closer to the experimental data.

Concerning the compression, only comparison for mean velocity are presented. As shown in Fig. 5, the development of secondary vortices is also evident from the PIV measurements. Unlike k–ε model which simply predicts a strong decay of the original vortex, RSM compares satisfactorily with the experiment during most of the compression. It must be noted however that the three-eddy pattern disappears gradually in the last part of compression in contrast with its reinforcement predicted by the model. Marc et al. (1997a) have noticed the existence of strong large-scale and cycle-dependent motions at this time of compression. The possibility that these facts could be connected will be also discussed in the next section.

4. Numerical simulation in laminar regime

Both turbulence models lead to similar mean velocity fields at the end of intake. However, predictions for the compression differ markedly. The first objective of this section is to illustrate by some direct numerical simulations that the differences obtained in the averaged levels of eddy viscosity at the end of intake (4 times higher in the case of k–ε model) are mainly responsible for these differences. Then, in the particular case of no-shear boundary conditions, we shall show that the compressed flow may exhibit strong three-dimensionality. Finally, we shall propose an explanation for the anomalous peaks of fluctuation detected at the end of intake.

As initial conditions when the compression starts, we take a 2D velocity field $\mathbf{v} = \nabla \times \psi\mathbf{z}$ with the streamfunction

$$\psi = \frac{b^2\Omega_o}{2\pi^2} \sin\frac{\pi x}{b} \sin\frac{\pi y}{b} \tag{10}$$

corresponding to one cell of the plane Taylor vortex flow. This particular field satisfies a zero-shear boundary condition rather than the no-slip one. However, as shown in Fig. 7(a), the deduced vorticity which is in the present case constant along streamlines is, except in the thin wall layers, a fairly good approximation of the vorticity fields deduced from the models. For these computations, the molecular viscosity is taken as a constant equal to the averaged value of the eddy viscosity. The Reynolds numbers $\mathrm{Re} = \Omega_o b^2/\nu$ based on the maximum value of the initial vorticity Ω_o is thus 1600 and 6000 corresponding respectively to k–ε and RSM models.

4.1. 2D simulations with no-slip boundary conditions

A first set of evolutions has been obtained imposing zero velocity on boundaries at initial time. In that case, viscous layers develop rapidly during the first steps of the computation. For the higher value of Re, separation occurs during compression and a final state consisting of three counterrotating eddies similar to the pattern observed in the case of $\overline{u_iu_j}$–ε model (Fig. 7(c)). For the lower value of Re, no clear separation is observed (Fig. 7(b)). The evolution is also similar to that obtained with the k–ε model. The meanflow decay is however stronger in the present case. This may be explained by

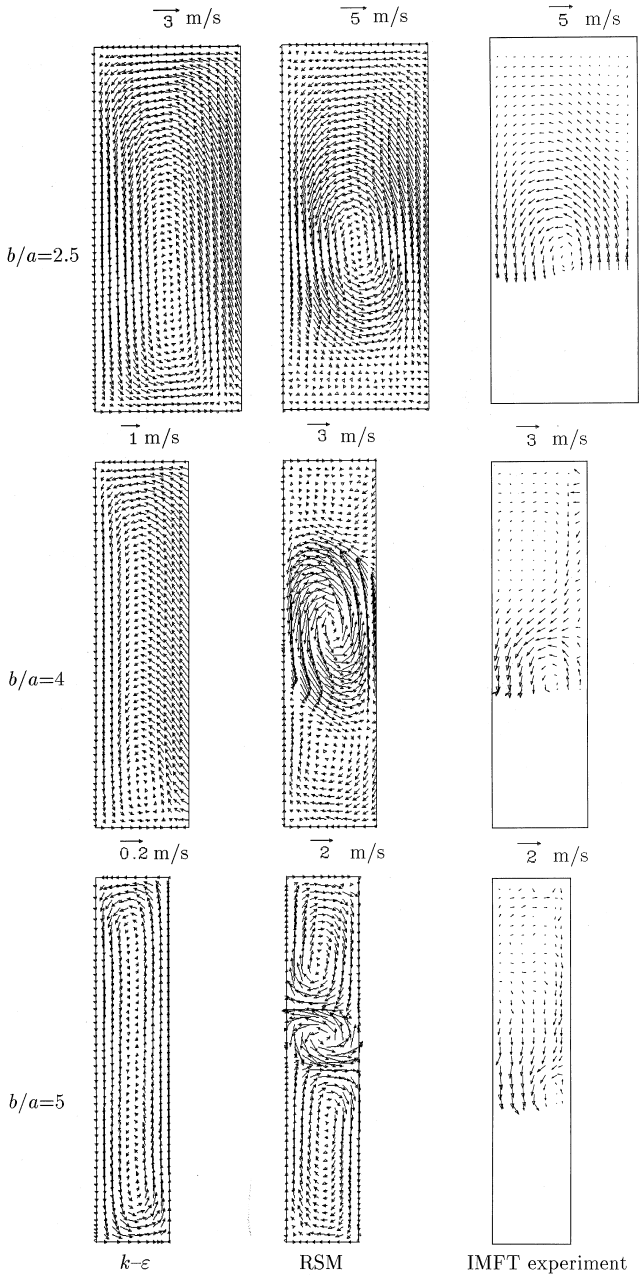

Fig. 5. Comparison models/experiment for velocity fields at volumetric ratio = 2.5, 4, 5.

the fact that ν_t decreases at the end of the compression whereas the molecular viscosity is assumed to be constant in the present case.

4.2. 3D simulations with shear-free boundary conditions

When the fluid is allowed to slip along the boundaries, one can find an analytical solution for the evolution of the Taylor vortex (Eq. (10)) during the compression. This solution reads

$$\mathbf{v} = \nabla \times \psi \mathbf{z} - \frac{1}{a}\frac{\mathrm{d}a}{\mathrm{d}t}\mathbf{x} \tag{11}$$

with

$$\psi = A(t)\sin\frac{\pi x}{a(t)}\sin\frac{\pi y}{b}, \tag{12}$$

$$A(t) = \frac{b^2\Omega_o}{\pi^2}\left(\frac{b}{a(t)}+\frac{a(t)}{b}\right)^{-1} \times \exp\left(-\nu\pi^2\int_0^t \mathrm{d}s\left(a(t)^{-2}+b^{-2}\right)\right). \tag{13}$$

When $a \neq b$ is a constant, this solution reduces to the flow studied by Lundgren and Mansour (1986). In that case, the solution is linearly stable under 2D disturbances and Mansour and Lundgren have proved the instability with respect to 3D perturbations when the Reynolds number is large enough. To some extent, this instability is similar to the three-dimensional instability of unbounded flow with elliptical streamlines (Bayly, 1986; Waleffe, 1990; Godeferd et al., 1996).

For the compressed Taylor vortex, a similar evolution may be expected. We have tested numerically the stability of this solution by introducing a small perturbation (1% of the main flow) consisting in a Taylor vortex similar to (Eq. (10)) with vorticity vector parallel to y axis. A Fourier pseudo-spectral code (64^3 modes) is used for this purpose and reflectional symmetries are assumed to ensure zero normal velocity conditions at the boundaries. Figs. 8 and 9 show surfaces of constant magnitude (one half of the maximum value) at four times during compression. At the initial time, the surface is aligned along z axis and the perturbation is not discernible. For the lower value of the Reynolds number, the perturbation is attenuated and the vorticity surface remains virtually identical to the case of unperturbed solution (Fig. 9). For the higher value, the perturbation is strongly amplified (Fig. 8). The initial sinusoidal shape of the perturbation steepens gradually. At the same time, the vorticity surface shrinks indicating some local amplification of the maximum vorticity. At the end of compression, this surface tilts suddenly towards negative z. Thus, one may conclude that the low value of the eddy viscosity given by RSM can give rise to substantial three-dimensional motion during the compression. In contrast, for the higher value corresponding to k–ε model, the Taylor vortex seems stable. These numerical experiments suggest that the transition to tridimensionality would occur at an intermediate value of the Reynolds number.

4.3. Precession of vortex core

As noted above, turbulence models cannot capture the local maxima of fluctuation in the center of the chamber. Marc et al. suggest that these peaks result from cyclic variations of the vortex center. We can refer to the dynamics of the Taylor vortex to test this hypothesis. For a square geometry ($a = b$), 2D linear eigenmodes of the non-viscous Taylor vortex are oscillatory. The lowest frequency mode ($0.16\Omega_o^{-1}$) corresponds to a precession motion of the vortex center. Reasonably, this first eigenmode may be approximated by a combination in quadrature of the first two harmonics of the basic stream-function (Eq. (10)). Averaging over the phase of this oscillating motion and assuming that the perturbation is small, the mean squared value of the fluctuation can be expressed as a function of the radius Δr of the trajectory of the vortex center. We have for x component

$$\overline{u^2} = \frac{\Delta r^2\Omega_o^2}{16}\left(2\sin^2\left(\frac{\pi x}{b}\right)\cos^2\left(\frac{2\pi y}{b}\right) + \frac{1}{2}\sin^2\left(\frac{2\pi x}{b}\right)\cos^2\left(\frac{\pi y}{b}\right)\right). \tag{14}$$

This identity, and the similar one for $\overline{v^2}$, are plotted in Fig. 6(b) and (c) with the value $\Delta r = 0.002$ m obtained from PIV measurements. Since the length scale of the vortex center motion is large compared to the integral length scale of the background

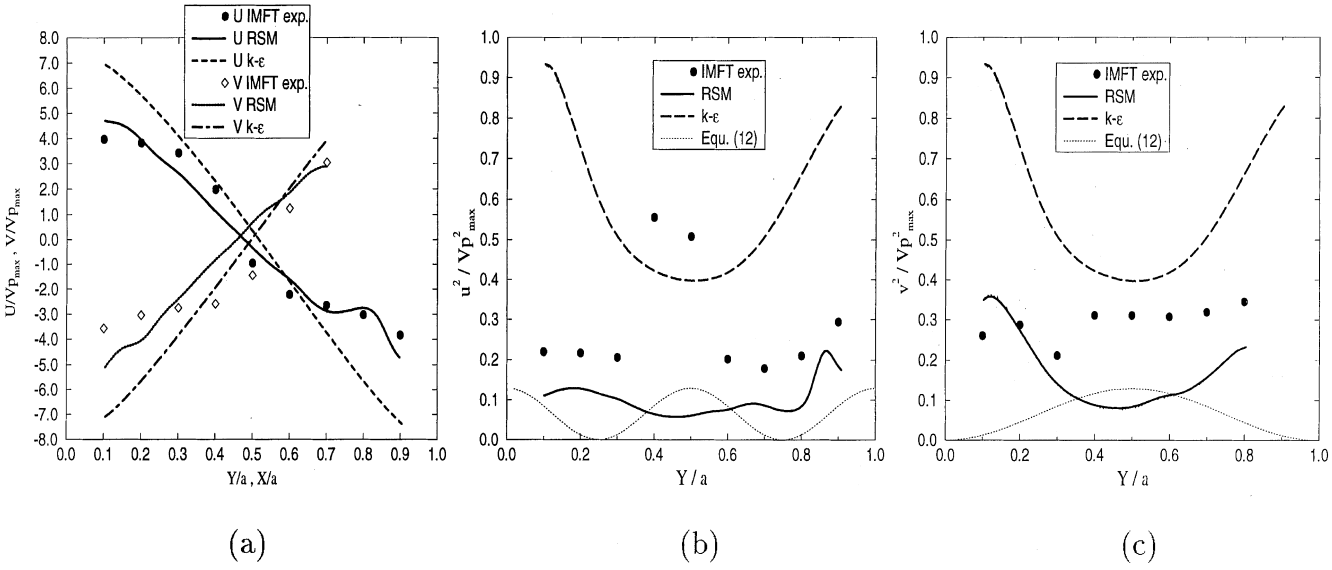

Fig. 6. Comparison IMFT experiment/model at 180°. (a) $U/Vp_{\max}$, $V/Vp_{\max}$. (b) $\overline{u^2}/Vp^2_{\max}$. (c) $\overline{v^2}/Vp^2_{\max}$.

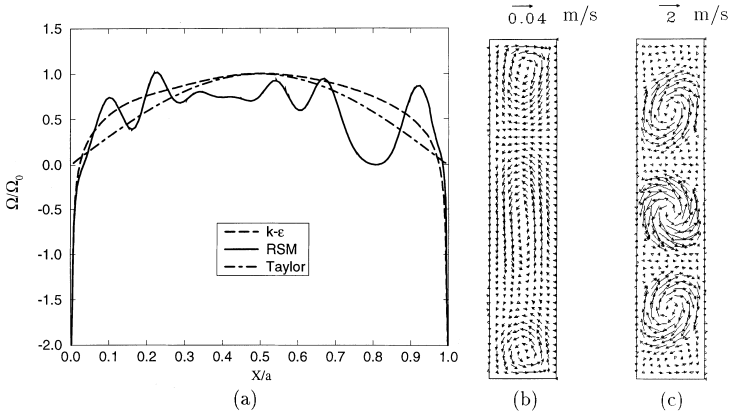

Fig. 7. Comparison models/Taylor for Ω/Ω_o at 180°: (a) Velocity at $\omega t = 360°$. (b) No-slip laminar case $\mathrm{Re} = 1600$. (c) No-slip laminar case $\mathrm{Re} = 6000$.

turbulence ($(\overline{u^2})^{3/2}/\varepsilon \sim 0.01$ m), one may consider that the corresponding contributions to the velocity are almost uncorrelated. Thus, it is tempting to filter the precession velocity by removing the mean-squared contribution from the total stress. Doing this, we cannot erase the central peak completely. One may consider however that the width and the maximum of the precession profile agree reasonably with the experimental data.

5. Conclusion

A numerical study of a turbulent vortex flow corresponding to Marc et al. (1997a) experiment is presented. First, 2D computations of the Reynolds-averaged equations with k–ε and $\overline{u_iu_j}$–ε models have been performed. During the intake, both models predict a well organized vortex with comparable angular momentum. During the compression, the evolutions of the mean flow are however dissimilar. Strong secondary vortices are by the $\overline{u_iu_j}$–ε model, whereas, in the case of k–ε model, we observe a rapid decay of the mean velocity in the late compression without significant secondary flow. This may be explained by the large difference between the eddy viscosity levels at the end of intake (4 times higher in the case of k–ε model), which in turn results from the well-known deficiency of k–ε models in swirling flows. This fact has been checked by direct numerical simulations with a constant viscosity equivalent the eddy viscosity of the models.

The experiment of Marc et al. shows that the main flow remains essentially two-dimensional during the intake. At the beginning of compression, kinetic energy levels lie between k–ε and $\overline{u_iu_j}$–ε predictions, with a better agreement however for the latter. The anomalous peaks of rms velocity detected in the center of the chamber are interpreted here in terms of precession of the vortex core. Some difference is observed with $\overline{u_iu_j}$–ε predictions in the second part of compression. The existence of three-dimensional and large-scale flow is suspected. Such an evolution that could be sensitive to perturbations in the initial state and thus cycle-dependant would have a smoothing effect on the average. Thus, an important question is to know if RSM computations or direct simulations with an equivalent viscosity could generate substantial three-dimensional flow. This 3D evolution could be generated by elliptical-type instability as illustrated by our direct simulations of the compressed

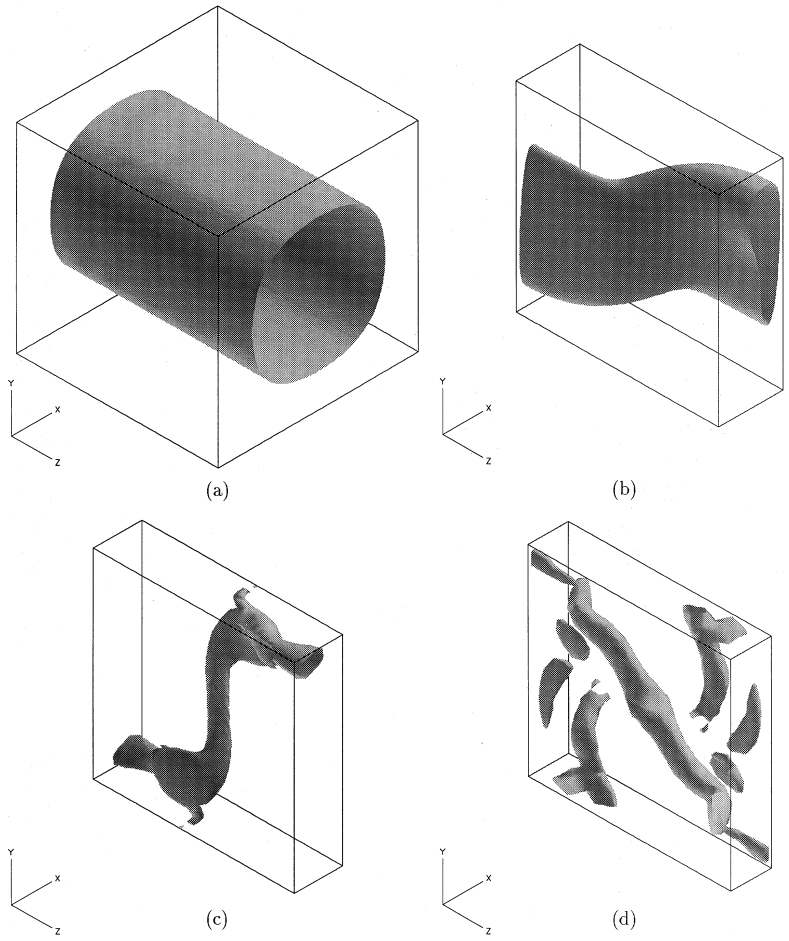

Fig. 8. Surfaces of magnitude of vorticity (half of maximum value) for Re = 6000: (a) $b/a = 1$; (b) $b/a = 3$; (c) $b/a = 4$; (d) $b/a = 5$. Ratios between maximum vorticity and maximum vorticity without perturbation are respectively 1, 1.38, 2.28, 1.39.

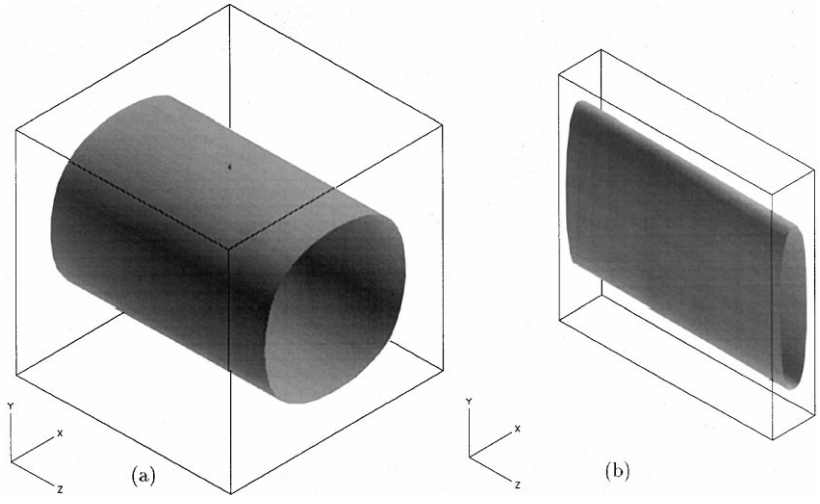

Fig. 9. Surfaces of magnitude of vorticity (half of maximum value) for Re = 1600. (a) $b/a = 1$. (b) $b/a = 5$. Ratios between maximum vorticity and maximum vorticity without perturbation are 1.

Taylor vortex. In these simulations, no-shear boundary conditions are used. With no-slip conditions, the stability of the flow may be rather different and further investigation is needed to verify this hypothesis.

Acknowledgements

This work was supported by CNRS-Ecotech, PSA and Renault in a joint program ARC "Combustion dans les

moteurs à piston''. O.L.R. has received a grant from the Agence pour le Développement et la Maîtrise de l'Energie (ADEME). We would like to thank M. Trinité, project coordinator, for his encouragement. We are grateful to D. Marc and J. Borée for providing us with new unpublished experimental data. We would also thank our colleagues at ECL, J.P. Bertoglio, M. Buffat, C. Cambon, D. Jeandel and J. Scott, for their interest in this work and stimulating discussions.

References

Bayly, B.J., 1986. Three-dimensional instability of elliptical flow. Phys. Rev. Lett. 57, 2160–2163.

Craft, T.J., Launder, B.E., 1991. Computation of impinging flows using second-moment closures. In: Eighth Symposium on Turbulent Shear Flows, Technical University of Munich.

Debaty, P., 1994. Performances des modèles de turbulence au second ordre appliqués à des configurations axisym étriques simulées par éléments finis. Thèse, Ecole Centrale de Lyon.

Gibson, M.M., Launder, B.E., 1978. Ground effects on pressure fluctuations in the atmospheric boundary layer. Journal of Fluid Mechanics 86, 49–511.

Godeferd, F.S., Mansour, N.N., Cambon, C., 1996. Compressing an elliptic vortex: Transition to turbulence by tumble breakdown. CTR Annual Research Briefs.

Launder, B.E., Reece, G.J., Rodi, W., 1975. Progress in the development of a Reynolds-stress turbulence closure. Journal of Fluid Mechanics 68, 537–566.

Lea, C.J., Watkins, A.P., 1997. Differential stress modelling of turbulent flows in reciprocating engines. In: Proceedings of Institution of Mechanical Engineers, vol. 211, Part D, pp. 59–77.

Lebrère, L., Buffat, M., Le Penven, L., Dillies, B., 1996. Application of Reynolds stress modelling to engine flow calculation. Journal of Fluid Engineering 118, 710–721.

Le Penven, L., Serre, G., 1996. Models of compressed turbulence (submitted to Journal of Fluid Mechanics).

Lundgren, T.S., Mansour, N.N., 1986. Transition to turbulence in an elliptic vortex. Journal of Fluid Mechanics 307, 43–62.

Mao, Y., Buffat, M., Jeandel, D., 1994. Simulation of the turbulent flow inside the combustion chamber of a reciprocity engine with a finite element method. Journal of Fluid Engineering 116, 363–369.

Marc, D., Borée, J., Bazile, R., Charnay, G., 1997a. Combined PIV and LDV analysis of the evolution and breakdown of a compressed tumbling vortex. In: 11th Symposium on Turbulent Shear flows, Grenoble, France.

Marc, D., Borée, J., Bazile, R., Charnay, G., 1997b. Tumbling vortex flow in a model square piston compression machine: PIV and LDV measurements. SAE Paper 972834.

Reynolds, W. C., 1980. Modelling of fluid motions in engine – An introductory overview. In: Combustion Modelling in Reciprocating Engine. Plenum Press, New York.

Serre, G., 1994. Etude expérimentale et modélisation de la turbulence homogène compressée. Thèse, Ecole Centrale de Lyon.

Speziale, C.G., Gatski, T.B., Mac Giolla Mhuiris, N., 1990. A critical comparison of turbulence models for homogeneous shear flows in a rotating frame. Physics of Fluids A 2, 1678–1684.

Waleffe, F., 1990. On three-dimensional instability of strained vortices. Physics of Fluids A 2, 76–80.

Watkins, A.P., Bo, T., 1996. Differential stress models for the simulation of swirling reciprocating model engine flows. In: Rodi, W., Bergeles, G. (Eds.), Proceeding of the Third International Symposium on Engineering Turbulence Modelling and Measurement, Crete, pp. 319–328.

Watkins, A.P., Lea, C.J., Gul, M.Z., 1991. Development of advanced turbulence models for the calculation of flows in I.C. engines cylinders. In: Proceedings of Institution of Mechanical Engineers International Conference on Computers in Engine Technology, Cambridge, C430/025, pp. 7–20.